minerals

MDPI

Article

Celestine Mineralisation in Jabal Hafit, Al-Ain (United Arab Emirates): Constraints from Geochemical and Sr-S Isotope Systematics

Mabrouk Sami [1,*], Bahaa M. Amin [1], Ioan V. Sanislav [2], Ahad Al-Ahbabi [1], Maryam Alali [1], Meera Malek [1], Mariam Aldhaheri [1], Aya Almenhali [1], Suhail S. Alhejji [3], Chun-Feng Li [4], Mostafa R. Abukhadra [1] and Douaa Fathy [5]

1 Geosciences Department, College of Science, United Arab Emirates University, Al Ain 15551, United Arab Emirates
2 Economic Geology Research Centre (EGRU), College of Science and Engineering, James Cook University, Townsville, QLD 4811, Australia; ioan.sanislav@jcu.edu.au
3 Geology and Geophysics Department, College of Science, King Saud University, Riyadh 11451, Saudi Arabia; salhejji@ksu.edu.sa
4 Department of Marine Science, Zhejiang University, Zhoushan 316021, China
5 Geology Department, Faculty of Science, Minia University, El-Minia 61519, Egypt; douaafathy@mu.edu.eg
* Correspondence: mabrouksami@uaeu.ac.ae

Abstract

Celestine ($SrSO_4$) is the principal ore of Sr and a sensitive tracer of diagenetic fluid–rock interaction in carbonate–evaporite successions. This study presents integrated petrographic mineral chemistry and Sr–S isotopic data for epigenetic celestine hosted by Asmari carbonates at Jabal Hafit, Al Ain (UAE), to constrain fluid source, and mechanisms of $SrSO_4$ precipitation during basin diagenesis. Field and SEM observations show celestine as stratabound, vug- and fracture-filling euhedral to subhedral crystals within dolomitised limestone, suggesting precipitation after initial lithification during early-to-mid burial diagenesis. Electron microprobe analyses show nearly stoichiometric $SrSO_4$ (55.15–57.30 wt.% SrO; 42.43–44.35 wt.% SO_3) with very low Ba and Ca. The characteristically high Sr/Ba signature of the celestine reflects a complex diagenetic history driven by efficient Sr remobilisation during carbonate recrystallisation within an inherently Ba-poor marine sequence. Measured $^{87}Sr/^{86}Sr$ ratios are tightly clustered (0.707841–0.707854) with a high degree of isotopic homogeneity, which indicates a stable, well-buffered fluid reservoir, while the absolute values align with an Oligocene marine signature. Sulphur isotope values ($\delta^{34}S$ = +27.3 to +29.1‰) are enriched relative to coeval marine sulphate, which could be attributed to closed-system Rayleigh fractionation driven by bacterial sulphate reduction. We propose that celestine precipitated from stable, marine-buffered burial brines, where supersaturation was achieved through coupled Sr enrichment from carbonate diagenesis and microbial modification of the sulphate reservoir.

Keywords: celestine; Asmari Formation; diagenesis; Sr isotopes; sulphur isotopes; Jabal Hafit; United Arab Emirates

Academic Editor: Georgia Pe-Piper

Received: 10 April 2026
Revised: 10 May 2026
Accepted: 23 May 2026
Published: 27 May 2026

1. Introduction

The formation of authigenic minerals within sedimentary basins provides a critical, highly detailed window into the complex physicochemical interactions that occur between migrating crustal fluids and host rock matrices over geological time [1,2]. Among these,

celestine ($SrSO_4$) is a key diagenetic mineral whose occurrence is often intimately linked to the evolution of marine evaporitic and carbonate sequences [3]. As the principal ore of strontium (Sr), its economic significance is matched by its value as a geochemical archive, recording the conditions of fluid flow, solute sources, and diagenetic environments long after primary deposition [1,4]. The precipitation of celestine requires specialised conditions: a source of Sr, a source of sulphate (SO_4), and a geochemical trigger such as fluid mixing or bacterial sulphate reduction (BSR) to achieve supersaturation [1,3,5]. This sensitivity to specific fluid chemistries and processes makes celestine a valuable archive of past fluid–rock interactions [4]. Understanding the genesis of such deposits is therefore crucial not only for economic geology but also for reconstructing paleo-fluid flow, diagenetic conditions, and the geochemical evolution of sedimentary basins.

The Earth's crust contains an average of 450 ppm Sr, making it the 15th most abundant element [4,6]. Despite this relative abundance, only two minerals, celestine and strontianite ($SrCO_3$), concentrate Sr at levels sufficient to form profitable, exploitable mineral deposits. While a completely solid solution exists theoretically between barite ($BaSO_4$) and celestine, natural occurrences exhibit a strongly bimodal distribution, with intermediate compositions being exceedingly rare. Because barite is orders of magnitude less soluble than celestine, any fluid containing equimolar or even moderately unequal amounts of Ba and Sr will precipitate barite first, rapidly stripping the fluid of barium [4,6]. Therefore, the formation of massive celestine deposits requires a mechanism to geochemically decouple Sr from Ba and Ca, concentrating the former while depleting or bypassing the latter [4,6].

Globally, major celestine deposits frequently occur within Cenozoic sedimentary successions, a geological era characterised by widespread evaporite formation across the Mediterranean, Paratethys, and Middle Eastern realms [7–10]. Deposits in Sicily, the Igualada Basin in Spain, and the Carpathian Foredeep in Poland exemplify a common genetic model where celestine precipitates from marine-derived brines that have undergone significant diagenetic modification [3,11,12]. In these settings, the interplay between seawater, evaporites, and organic matter drives processes like BSR, which preferentially removes the lighter ^{32}S isotope from the sulphate reservoir, leaving behind ^{34}S-enriched sulphate that is subsequently incorporated into celestine. Concurrently, Sr isotope ratios ($^{87}Sr/^{86}Sr$) can be used to fingerprint the fluid source and, due to the well-defined evolution of the marine $^{87}Sr/^{86}Sr$ curve through the Cenozoic, provide a powerful tool for geochronology [13,14]. The Middle East, with its extensive Cenozoic carbonate–evaporite platforms, hosts analogous deposits, such as those in the Zagros Fold Belt of Iran [6], suggesting that the processes governing celestine formation are widespread in these tectonic and stratigraphic settings.

The Jabal Hafit anticline, a prominent geological structure in the Al-Ain city of the United Arab Emirates (UAE), represents an ideal natural system to investigate these processes. This NNW-SSE-trending, doubly plunging anticline is a unique structural feature, exposing a thick succession of Eocene to Miocene sedimentary rocks [15]. The stratigraphy is dominated by the carbonates and marls of the Rus, Dammam, and Asmari Formations, which are overlain by a Miocene evaporitic sequence [15–17].

Celestine is recorded within the Asmari Formation, and despite its recognition as a notable mineral occurrence, its genesis remains poorly constrained. Previous studies have primarily focused on field descriptions and preliminary observations [15–18], leaving fundamental genetic questions unresolved. The precise source of the mineralising fluids, whether they were unmodified Oligocene seawater, evolved basinal brines, or possessed a hydrothermal component, remains unclear. The specific mechanisms responsible for mobilising Sr and SO_4, and the trigger for their co-precipitation as celestine, have not been rigorously determined. Furthermore, the mineralisation process relative to the deposition and diagenetic history of the Asmari Formation is poorly constrained.

To bridge this knowledge gap, the present study employs a multi-proxy analytical approach to construct a robust genetic model for the Jabal Hafit celestine deposit. This integrates detailed field, microtextural features, mineral chemistry and Sr and S isotopic data to determine the origin of the mineralising fluids and the dominant geochemical processes that control $SrSO_4$ supersaturation. The findings will not only clarify the origin of celestine deposits in the UAE but will also contribute to the understanding of celestine genesis in carbonate–evaporite systems, with implications for basin analysis, diagenetic modelling, and mineral exploration.

2. Geological Background

2.1. Regional Geology of the UAE

The UAE is located in the southeastern part of the Arabian Peninsula in the Middle East. It lies on the eastern margin of the large Arabian Plate, bordered by distinct tectonic boundaries (Figure 1a), which has remained relatively tectonically stable throughout the Phanerozoic. Although Quaternary sediments cover a large portion of the UAE [19], the Hajar Mountains, the Musandam Peninsula to the east, and western Abu Dhabi feature significant outcrops of bedrock (Figure 1b). These thick successions of Palaeozoic–Cenozoic sedimentary deposits are underlain by deeply buried Precambrian basement rocks [20].

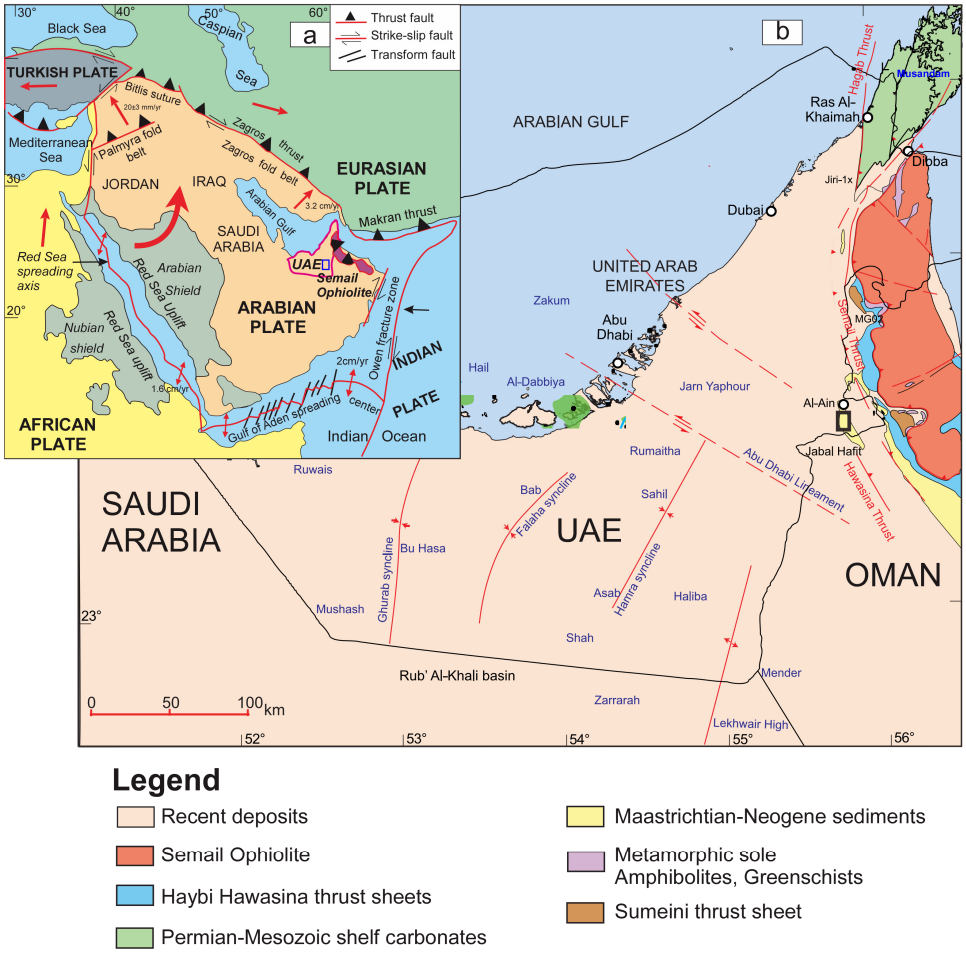

Figure 1. (**a**) Regional geological map of the Arabian Plate showing the location of the UAE; (**b**) simplified geological map of the UAE, showing the location of Jabal Hafit.

During the Palaeozoic, the Afro-Arabian plate shifted through high latitudes, including glaciation phases in the Ordovician–Silurian, before entering more tropical settings in the Mesozoic and Cenozoic. Throughout the Cenozoic, the UAE experienced additional

deposition in shallow marine and sabkha environments, followed by desertification and the formation of dunes. The Quaternary period saw the development of modern surface environments, including sabkhas along the coast and dune fields inland. Evaporitic deposits such as celestine are widespread across the Emirate of Abu Dhabi, with their most prominent surface exposures located on the eastern flank of the Jabal Hafit anticline, in addition to being accessible for study in various quarries [8,16].

2.2. Local Geology and Field Features

The Al-Ain city, in eastern Abu Dhabi, overlies a Cretaceous–Palaeogene foreland-basin succession that records the flexural response of the Arabian margin to ophiolite obduction and subsequent convergence. The surface is largely mantled by mobile eolian sands. Tectonically, the region is significantly influenced by the Semail Ophiolite, representing obducted oceanic crust and mantle material [21]. This tectonic activity is evidenced by active faults and thrust faults. The area of Al-Ain is divided into three primary geomorphic provinces: (1) the southeastern Jabal Hafit hills, (2) the Al-Jawa piedmont plain to the east, and (3) the dune-covered scarps found to the north and south. A dominant geological characteristic of this region is the foothills of the northern Oman Mountains, which include Jabal Hafit and other prominences such as Jabals Auha, Huwayyah, Malaqet, and Mundassah. While Mesozoic rocks are exposed at Jabal Mundassa to the east, the rock sequence at Jabal Hafit is notably younger, belonging to the Tertiary period [22].

Jabal Hafit stands as the most prominent geomorphic feature in the region. It is approximately 29–30 km long and 5 km wide, rising to an elevation of ~1160 m, forming an elongated NNW–SSE trending ridge located about 17 km west of Jabal Malaqet and southeast of Al-Ain city (Figure 2a). Structurally, it is an eroded, asymmetrical, doubly-plunging anticline, partly overturned and locally overthrust towards the east, interpreted as an upthrusted fault-bend fold formed during the Zagros Orogeny [15]. This orogenic event, driven by the collision between the Arabian and Eurasian plates from the late Eocene to Oligocene, resulted in the closure of the Neo-Tethys Ocean [23]. The sedimentary succession forming the anticline was deposited after the emplacement of the ophiolite nappes. Jabal Hafit anticline is cut by NE–SW- and N–S-striking high-angle faults and subordinate E–W-striking strike-slip faults (Figure 1a). The western limb is steep and locally overturned, whereas the eastern limb dips more gently towards the Al-Jawa plain, where Miocene evaporites are preserved in the back-limb and fore-limb positions (Figure 2a).

The exposed stratigraphic succession at Jabal Hafit ranges from Late Cretaceous to Miocene (Figure 2b). At the base, blocks of Semail Ophiolite (serpentinite and peridotite) are overlain by thin, ophiolite-derived conglomerates of the Qahlah Formation and shallow-marine bioclastic limestones of the Simsimah Formation. These are succeeded by marls with conglomeratic interbeds of the Muthaymimah Formation and a thick Palaeogene carbonate platform succession. The lowermost Palaeogene unit is the Rus Formation, comprising ~200 m of grey, thick-bedded, dolomitic and nodular limestone with chert bands and nodules; it is pervasively fractured and cavernous. Above, the Dammam Formation consists of several hundred metres of thin-bedded, hard, nummulitic limestones alternating with softer marls, forming the bulk of the core of the anticline. These Eocene carbonates pass upwards into Oligocene shallow-marine carbonates and marls assigned to the Asmari Formation, which form the principal host for celestine mineralisation. The Miocene succession on the eastern flank begins with the evaporite-rich Lower Fars Formation, overlain by syn-tectonic conglomerates of the Barzaman Formation and unconsolidated Quaternary aeolian sands and gravels (Figure 2b).

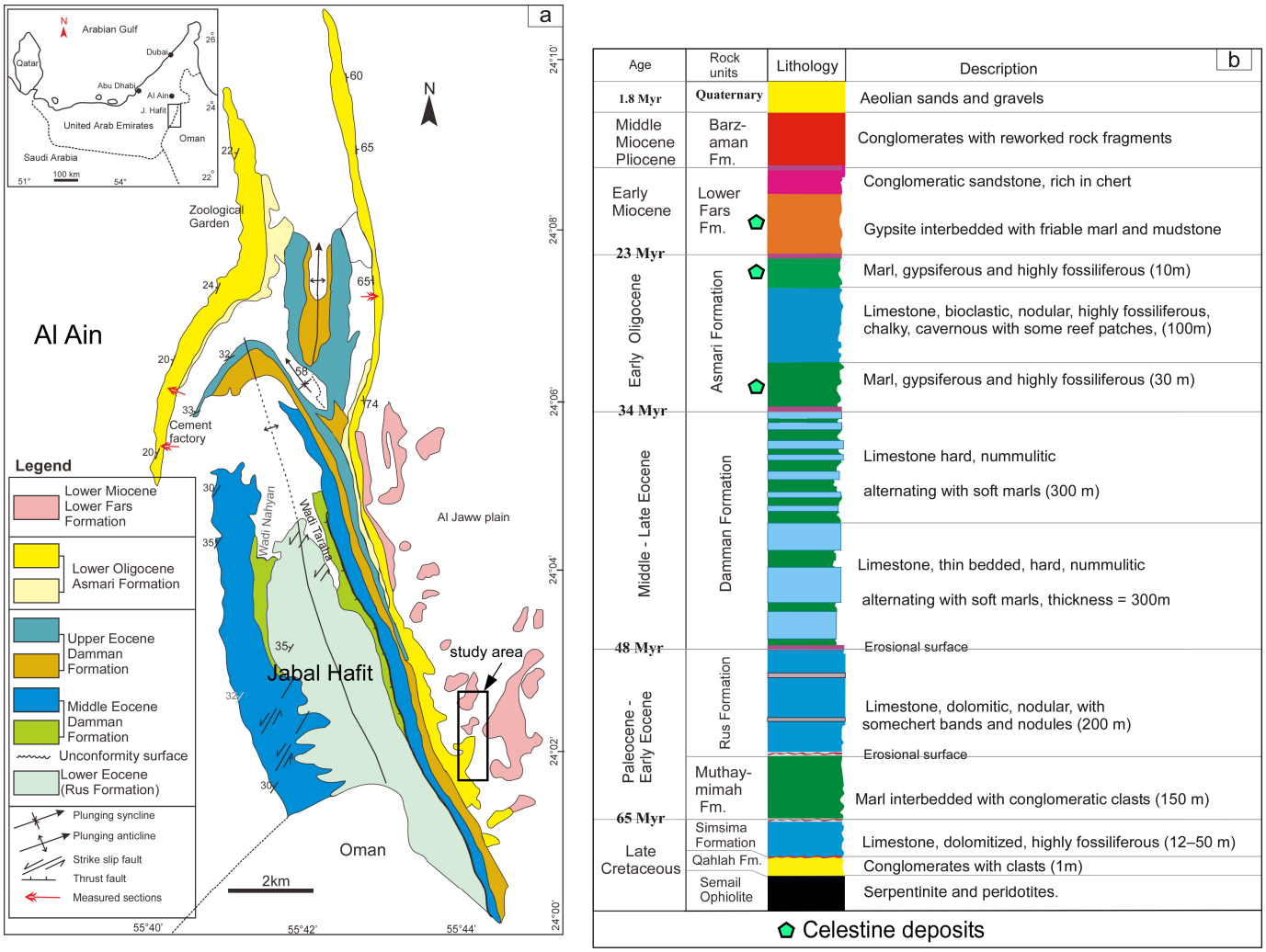

Figure 2. (**a**) Geological map of the Jabal Hafit and its surroundings; (**b**) stratigraphic framework of lithostratigraphic units exposed in the Jabal Hafit area (modified from Arman et al. [24]).

Celestine was first documented on the eastern limb of the Jabal Hafit anticline as a laterally persistent horizon at the base of the Miocene gypsum-bearing succession. This band is typically 10–20 cm thick but locally attains ~1 m, forming a distinctive stratigraphic marker along several kilometres of the eastern flank. Field photographs (Figure 3a–c) show that celestine occurs as massive, coarse-grained aggregates and lenses developed within Asmari carbonates. In outcrop, the celestine forms irregular, decimetre-scale, stratabound bodies with undulating upper and lower surfaces, locally coalescing into metre-scale pods. Individual crystals are colourless to pale yellow, commonly bladed or tabular, and some exceed several centimetres in length. The limestone–marl beneath the celestine is highly fractured, with fractures filled by celestine and fibrous gypsum. celestine masses contain fragments of limestone and gypsum [16].

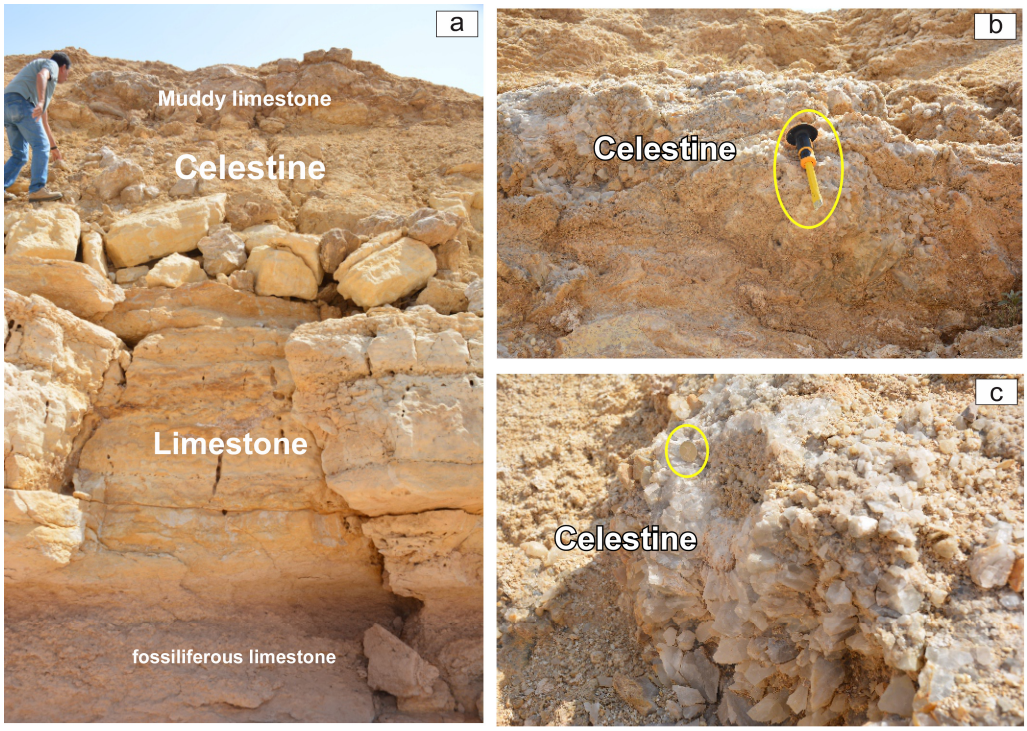

Figure 3. (**a**) Stratigraphic section showing fossiliferous limestone, the celestine layer, and the muddy limestone cap. (**b**,**c**) Euhedral celestine crystals in fluid-filled cavities, indicating epigenetic formation. The yellow circle refers to scale.

3. Analytical Methods

Samples were collected from the laterally persistent celestine horizon exposed on the eastern flank of Jabal Hafit. Twelve separate purified celestine samples (HC1–HC12) were analysed for Sr and S isotopes. Representative polished thin sections and grain mounts from samples HC5, HC9 and HC10 were used for quantitative mineral chemistry, yielding 21 spot analyses of celestine and 12 analyses of associated carbonates (six calcite and six dolomite). Quantitative mineral chemistry was obtained using an electron microprobe JEOL JXA (kishima, Tokyo, Japan) on thin polished sections and grain mounts of the celestine and carbonate samples.

A JEOL JXA series EMPA instrument (Wuhan Sample Solution Ltd., Wuhan, China) was operated at an accelerating voltage of 15 kV and a beam current of 10 nA, with a focused beam for celestine and a slightly defocused beam (5 μm) for carbonates to minimise the volatilisation of CO_2. Natural and synthetic standards were used for calibration (e.g., barite for Ba and S, strontianite for Sr, calcite for Ca, periclase for Mg and hematite for Fe). The following elements (reported as oxides) were analysed: CaO, SrO, BaO, MgO, FeO, MnO, Na_2O, K_2O, TiO_2, SiO_2, Al_2O_3, P_2O_5 and SO_3. For celestine grains, CO_2 was not applicable; for carbonate minerals, CO_2 was calculated by difference, assuming that all charge balance not accounted for by cations is due to CO_3^{2-}. Typical analytical precision was better than 1% relative for major oxides, and detection limits were on the order of 0.01 wt.% for most elements.

For Sr isotopic analysis, high-purity celestine separates were dissolved in 6 M HCl, and carbonate matrix samples in 2% HNO_3, in Savillex beakers. Strontium was isolated using standard ion-exchange column chromatography (Sr-spec resin) to remove Rb and other matrix elements. The $^{87}Sr/^{86}Sr$ ratios were measured on a Thermal Ionisation Mass Spectrometer (TIMS) (ThermoFisher, Waltham, MA, USA) in dynamic mode, with an internal precision of $<\pm 5 \times 10^{-6}$ (2σ) at the Wuhan sample solution lab (China). Repeated

analysis of NIST SRM-987 yielded $^{87}Sr/^{86}Sr = 0.710250 \pm 0.000012$ (2σ), confirming long-term accuracy. All reported sample ratios were normalised to $^{88}Sr/^{86}Sr = 8.375209$ and corrected for instrumental fractionation; the results were also adjusted to the SRM-987 value of 0.710250. Typical total procedural blanks for Sr were <1 ng and negligible. Because the long-term external reproducibility of SRM-987 is ±0.000012 (2σ), inter-sample differences of similar magnitude are not interpreted as analytically resolvable unless independently supported by superior within-run precision.

Celestine $\delta^{34}S$ was determined to evaluate the sulphur source and any isotopic fractionation effects (Wuhan Sample Solution Ltd., Wuhan, China). Approximately 5–10 mg of pure celestine from each sample was reacted with an excess of NaCN in a Teflon vessel to convert sulphate to thiocyanate, which was then acidified to release H_2S. The H_2S was trapped as Ag_2S by bubbling through a silver nitrate solution. The recovered Ag_2S was filtered, washed, dried, and weighed. Sulphur isotope ratios were measured on the Ag_2S using a Flash Elemental Analyser coupled to an IRMS (isotope ratio mass spectrometer) (Thermo Fisher Scientific, Bremen, Germany) in continuous flow mode, or by conventional combustion of Ag_2S to SO_2 followed by dual-inlet IRMS. Results are reported in δ notation as per mil (‰) deviations of the $^{34}S/^{32}S$ ratio from the Vienna Canyon Diablo Troilite (V-CDT) standard. Two international sulphate standards (NBS-127, $\delta^{34}S = +20.3‰$; IAEA-SO-5, $\delta^{34}S = +0.5‰$) were processed alongside samples to calibrate the measurements. The analytical reproducibility for $\delta^{34}S$ was better than ±0.2‰ (1σ). Celestine yields were quantitative, and no isotope fractionation is expected in the chemical conversion, as verified by replicate analyses.

4. Results and Discussion

4.1. Mineralogical and Microtextural Characteristics

Field observations (Figure 3a–c) show that celestine is an epigenetic phase hosted by lithified Asmari carbonates. It occurs mainly as vug- and fracture-filling crystals within dolomitised limestone rather than as primary depositional laminae. The open-space habit, well-developed crystal terminations, fracture–fill relationships and incorporation of host-rock fragments indicate precipitation after lithification, when the carbonate had already developed secondary porosity and brittle permeability. These features are incompatible with a syndepositional or unconsolidated sediment setting but are fully consistent with burial-diagenetic mineralisation in post-lithification fractures and cavities [25]. The translucent, elongate-prismatic to bladed habit further indicates precipitation from Sr-rich fluids migrating through the host carbonate [6].

Photomicrographs (Figure 4a,b) and SEM–BSE imaging (Figure 4c–f) refine these field relationships. The photomicrographs show coarse tabular to prismatic celestine crystals embedded within an interstitial carbonate matrix composed mainly of calcite–dolomite (Figure 4a,b). In PPL, celestine appears colourless to pale grey with moderate to high relief, prominent cleavage, and abundant internal fractures. Under XPL, the same crystals display bright interference colours and irregular extinction, reflecting cleavage-controlled deformation and microfracturing. Carbonate phases occur as a cloudy matrix and grain-boundary/seam-filling material between celestine crystals, suggesting late-stage carbonate infill and/or partial replacement associated with fluid-assisted crystallisation.

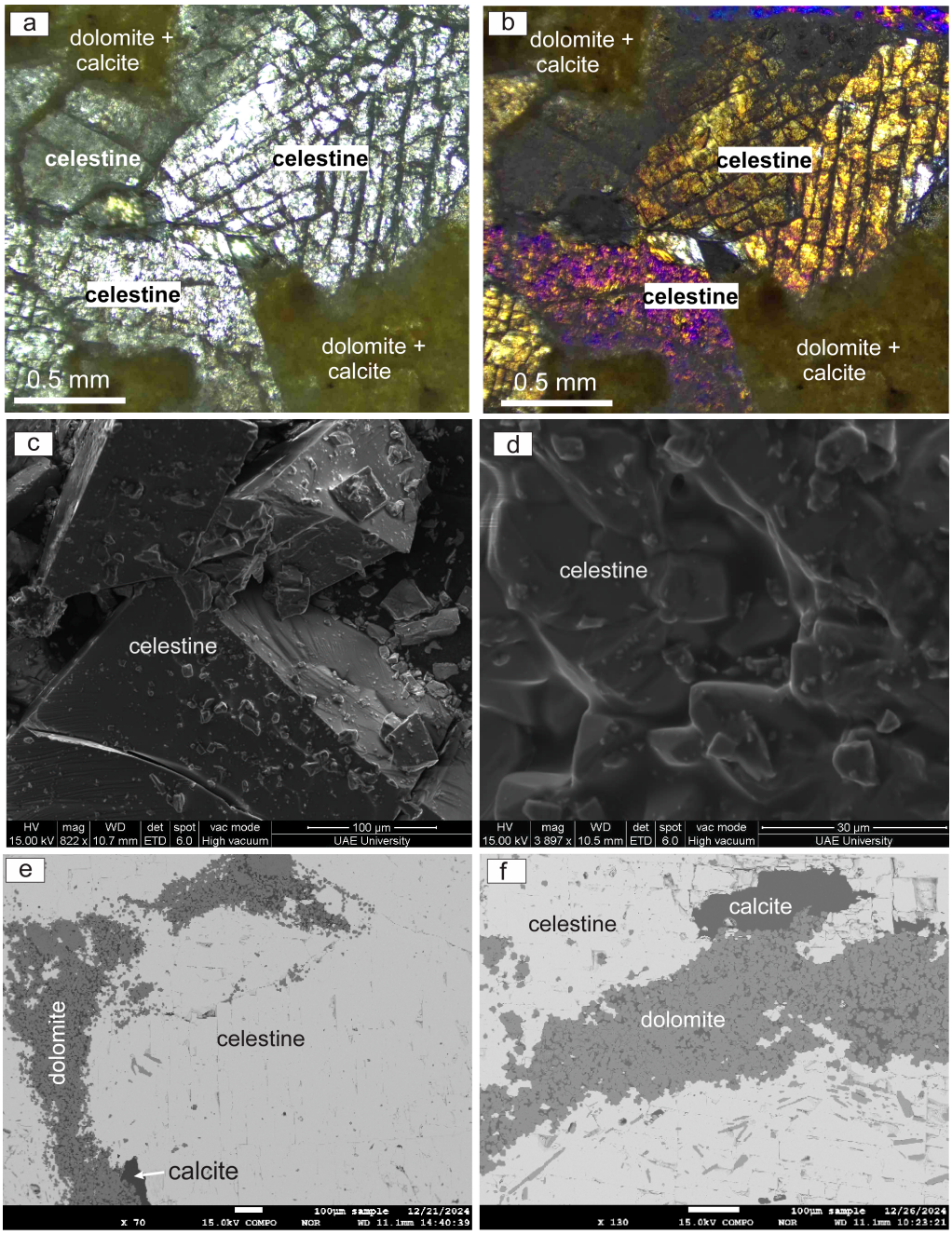

Figure 4. Photomicrographs, SEM and BSE images showing celestine texture and paragenetic relationships. (**a**,**b**) Paired PPL–XPL photomicrographs showing fractured tabular celestine, highlighted in cyan, within an interstitial calcite–dolomite carbonate matrix. (**c**,**d**) Euhedral celestine crystals filling open space. (**e**,**f**) Celestine in contact with dolomite and calcite within secondary porosity.

In SEM and BSE images (Figure 4c–f), celestine forms euhedral to subhedral tabular aggregates that line and fill secondary pores and fractures generated during diagenetic modification of the host carbonate. Celestine crystals nucleate on or between planar-euhedral dolomite rhombs in vugs, indicating that celestine precipitation overlapped with, or slightly post-dated, late dolomite growth. The drusy cavity-filling textures confirm crystallisation in open, fluid-filled voids under burial conditions rather than by surface weathering [26]. Calcite occurs as sparry patches or veins truncating the dolomitic mosaic, and carbonate adjacent to celestine-filled fractures shows recrystallised faces oriented toward the fracture margins, indicating that mineralisation was linked to post-lithification recrystallisation and fluid flow. No karst-related replacement textures or late weathering

overgrowths were observed. These textures place celestine precipitation within a burial-diagenetic paragenesis after brittle porosity had developed.

4.2. Geochemical Signatures and Implications for Fluid Sources

Powder X-ray diffraction (XRD) analysis of hand-picked celestine (Supplementary Figure S1) yields a pattern characterised by sharp, high-intensity reflections, indicating a well-crystalline phase. The quantitative chemical composition of the Jabal Hafit celestine, as determined by electron microprobe analysis (EMPA), reveals a phase of remarkable stoichiometric purity. The data, presented in Supplementary Table S1 and plotted in Figure 5a–d, show that SrO concentrations range from 55.15 to 57.30 wt.% with a mean of 56.10 ± 0.46 wt.%, while SO_3 concentrations vary between 42.43 and 44.35 wt.% with a mean of 43.47± 0.49 wt.%. The calculated structural formulae yield an average of 0.99 ± 0.01 apfu for Sr and 1.00 ± 0.01 apfu for S. These values closely approach the ideal stoichiometry of $SrSO_4$, with very low standard deviations and minimal interference from minor elements like Ba or Ca. Moreover, the trace elements in celestine, including Na_2O, K_2O, MnO, and TiO_2, are consistently below 0.05 wt.%, indicating that the crystal lattice retained limited chemical substitution throughout its growth.

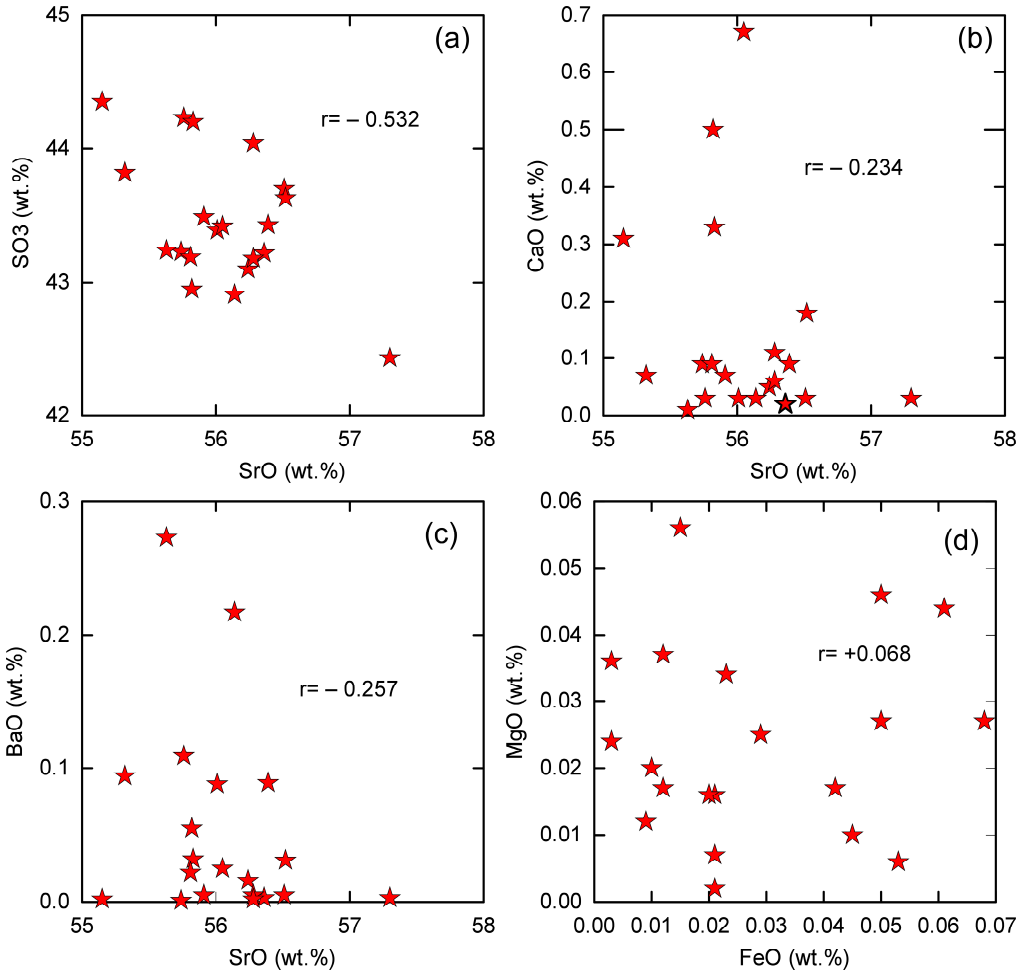

Figure 5. Bivariate plots of mineral chemistry in Jabal Hafit celestine: (**a**) SO_3 versus SrO, showing analytical data clustering tightly around the theoretical stoichiometric composition of pure celestine. The slight dispersion around the ideal centre is primarily attributed to minor isomorphous substitutions and analytical variance. (**b**) CaO vs. SrO and (**c**) BaO vs. SrO, displaying the very low levels of Ca and Ba substitution for Sr. (**d**) MgO vs. FeO, showing no systematic correlation, suggesting that these elements are present as trapped trace impurities rather than lattice-bound cations.

Both the oxide plots (Figure 5a–d) and the calculated formulae indicate only minor substitution by Ca and Ba on the Sr site. SrO and SO_3 contents vary only within a narrow range and show at most a weak inverse trend (Figure 5a), which is consistent with minor analytical scatter and/or limited coupled substitution rather than major deviation from the ideal formula. Minor-element plots (e.g., SrO–CaO, SrO–BaO; Figure 5b,c) display low but detectable Ca and Ba contents, without strong systematic covariance with SrO. This suggests restricted isovalent substitution of Ca^{2+} and Ba^{2+} on the Sr^{2+} site, producing only a very limited solid solution toward anhydrite or barite [25].

The weak negative trend between BaO and SrO (correlation coefficients (r) = −0.257), coupled with very low Ba concentrations, suggests minimal solid solution and precipitation from fluids with a high Sr/Ba ratio. This elevated Sr/Ba signature is characteristic of fluids that have evolved in marine or saline environments, where soluble Sr is enriched relative to Ba, which is efficiently scavenged through barite precipitation [27]. This aligns with measured BaO values that rarely exceed 0.27 wt% (≤0.004 apfu), indicating that the diagenetic fluids were strongly Sr-rich and Ba-poor, consistent with brines derived from marine evaporites [4]. The high Sr/Ba ratios observed in the Jabal Hafit celestine are consistent with mineralisation derived from marine-influenced brines. However, this signature likely reflects a complex diagenetic history rather than a simple primary marine precipitate. The conversion of metastable, Sr-rich marine carbonates (aragonite/high-Mg calcite) to stable low-Mg calcite is a well-documented 'Sr-pump' that enriches pore fluids in strontium [1]. When these Sr-enriched fluids mixed with sulphate-rich waters, potentially derived from the dissolution of nearby evaporitic units, the high Sr/Ba ratio was maintained due to the inherent Ba depletion of the host marine sequence and the higher solubility of celestine relative to barite. Thus, the observed geochemical patterns are the cumulative result of carbonate recrystallisation and fluid mixing within a stable, marine-derived reservoir.

The absence of correlation between MgO and FeO (Figure 5d) suggests that these trace elements are likely hosted in detrital impurities or fluid inclusions, rather than incorporated into the celestine structure itself. This observation aligns with established crystal-chemical principles, which indicate that the ionic characteristics of Mg^{2+} and Fe^{2+}/Fe^{3+} are incompatible with direct substitution for Sr^{2+} in the celestine lattice [28,29]. This chemical homogeneity points to a stable, well-buffered fluid reservoir during the mineralisation event [28,29].

Geochemical compositions of associated carbonate phases (calcite and dolomite) from the Jabal Hafit area are presented in Supplementary Table S2 and illustrated in Figure 6a–d. Their geochemical signatures stand in clear contrast to the patterns observed in the associated celestine. In the carbonates, SrO is consistently a minor component (≤0.23 wt%), showing no correlation with the major cations (Figure 6a–d). Calcite is distinguished by its high CaO content and very low MgO, while dolomite shows the characteristic coupled CaO and MgO with no relationship to SrO (Figure 6a,b). Calcite contains 54.11–55.67 wt% CaO with <1 wt% MgO, whereas dolomite exhibits ~29–30 wt% CaO and ~21–22 wt% MgO, confirming near-stoichiometric compositions and revealing the ferroan character of the dolomite (Fe = 0.009–0.015 apfu) [30]. This confirms that Sr does not significantly substitute for Ca or Mg in the carbonate lattices [31]. The very low concentrations of BaO in both carbonates align with its behaviour as a trace element in this system.

A noteworthy observation is the small amount of sulphate detected in the calcite and dolomite, showing 0.06%–0.18% SO_3 in the carbonates. These values suggest that some sulphate was retained either within the lattice as carbonate-associated sulphate or in microfluid inclusions, indicating that sulphate-bearing fluids coexisted with carbonate precipitation [32,33]. The presence of SO_3 in dolomite supports the idea that dolomitisation

and sulphate influx were contemporaneous, reflecting the interplay of sulphate-rich fluids and carbonate mineralisation during diagenesis [34].

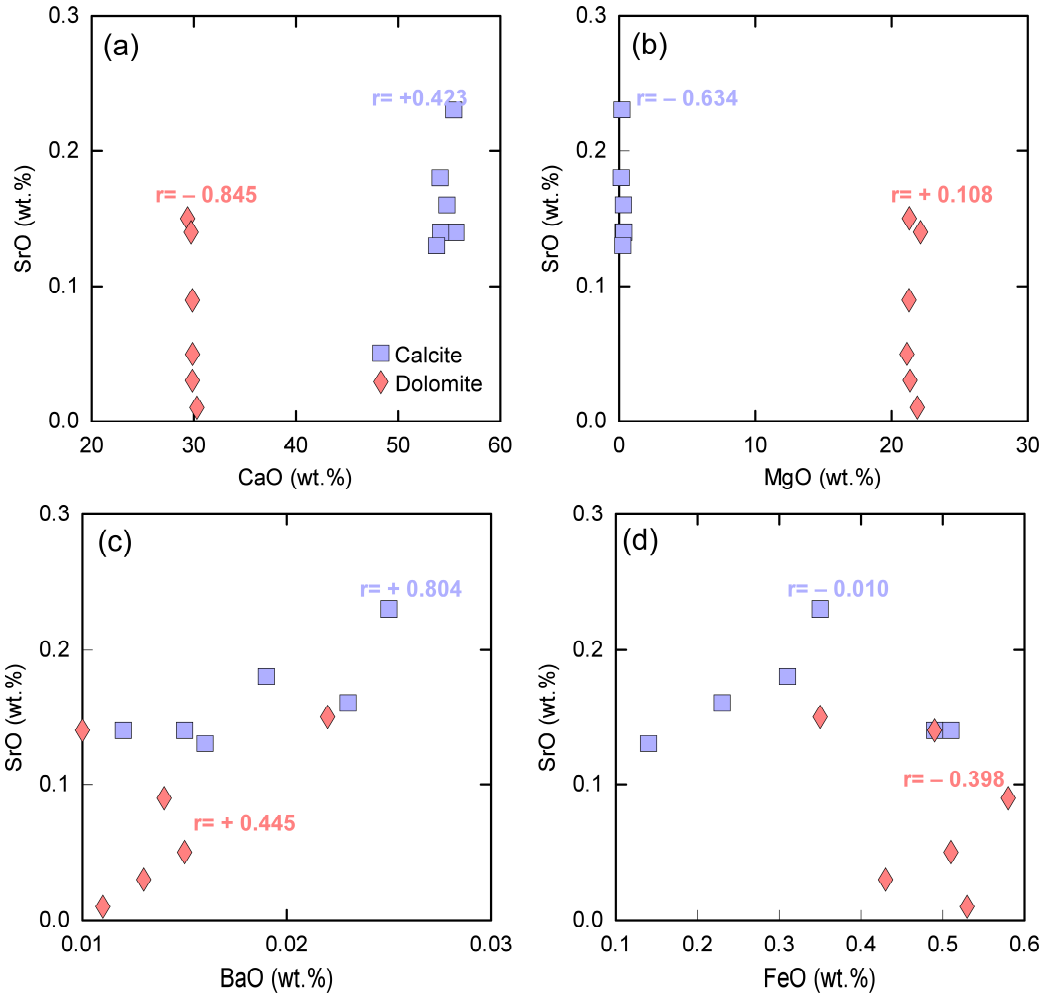

Figure 6. Bivariate plots of key oxides in calcite and dolomite from the Jabal Hafit area: (**a**) SrO vs. CaO; (**b**) SrO vs. MgO; (**c**) SrO vs. BaO; and (**d**) SrO vs. FeO. Both carbonate phases contain only trace Sr, supporting late Sr remobilisation during diagenesis.

In general, the carbonate and celestine geochemistry indicate early carbonate cementation followed by fracture-controlled precipitation of celestine from evolved diagenetic brines. The contrast between trace Sr in calcite–dolomite and the Sr-rich celestine emphasises efficient Sr remobilisation during burial fluid–rock interaction.

4.3. Sr and S Isotope Signatures and Constraints on Fluid Source

Strontium isotopes are particularly useful for identifying marine versus non-marine fluid reservoirs because the $^{87}Sr/^{86}Sr$ ratio of seawater is globally homogeneous at any given time owing to the long residence time of Sr in the ocean relative to the ocean-mixing time [13,14]. For diagenetic minerals, however, Sr-isotope stratigraphy is best treated as a broad stratigraphic constraint rather than a strict geochronometer because fluid–rock exchange and delayed cementation may decouple precipitation age from the marine curve.

The celestine samples yield exceptionally tightly clustered $^{87}Sr/^{86}Sr$ ratios of 0.707841–0.707854 (mean 0.707847; n = 12) (Table 1). Notably, the total spread of 0.000013 is statistically indistinguishable from the long-term external reproducibility of the NIST SRM-987 standard (±0.000012, 2σ). Consequently, these data are characterised by their isotopic homogeneity, which indicates precipitation from a single, well-buffered fluid reser-

voir rather than discrete fluid events. While this uniformity precludes high-resolution internal stratigraphic differentiation, the absolute values remain highly diagnostic; they overlap the Oligocene marine Sr curve and are broadly compatible with an Asmari-age marine signature. This suggests a dominant marine-buffered source with only negligible contributions of radiogenic Sr from siliciclastic detritus or deep crustal fluids.

Table 1. Sr and S isotopic compositions of celestite from Jabal Hafit, Al-Ain, UAE, with Standard Reference Values for the sulphur isotope.

Sample ID	$^{87}Sr/^{86}Sr$	2SE	Numeric Age (Ma) *	$d^{34}S_{V\text{-}CTD}$‰
HC1	0.707842	0.000012	30.17	28.78
HC2	0.707847	0.000011	30.10	28.56
HC3	0.707850	0.000009	30.05	27.94
HC4	0.707849	0.000011	30.06	28.09
HC5	0.707848	0.000010	30.08	29.07
HC6	0.707844	0.000010	30.15	28.60
HC7	0.707854	0.000009	29.98	27.28
HC8	0.707852	0.000012	30.01	27.65
HC9	0.707841	0.000014	30.23	29.08
HC10	0.707850	0.000008	30.04	29.03
HC11	0.707843	0.000010	30.17	27.99
HC12	0.707846	0.000010	30.11	28.44
Standard			Measurement value $d^{34}S_{V\text{-}CTD}$‰	Recommended value $d^{34}S_{V\text{-}CTD}$‰
SO-5			0.48	0.49 (n = 6)
SO-6			−34.07	−34.05 (n = 6)
NBS127			21.11	21.12 (n = 6)

* $^{87}Sr/^{86}Sr_i$ values were used to calculate the numerical age according to the following numerical age (Ma) = $^{87}Sr/^{86}Sr - 0.70974/-0.0000629$.

If compared cautiously with the LOWESS marine Sr curve, the measured ratios are broadly compatible with Oligocene, probably Rupelian, seawater-like compositions (Figure 7). However, the Oslick–Flecker regressions were calibrated for well-preserved marine carbonates and are not applied here as a precise geochronometer for diagenetic celestine. Accordingly, we do not treat the Jabal Hafit data as defining a numerical mineralisation age; instead, they provide a broad stratigraphic constraint consistent with precipitation during early-to-mid burial of the Asmari succession. Marine-derived fluids remain the most consistent interpretation for the Jabal Hafit celestine formation. A shallow-burial, marine-buffered brine is considered the most plausible model on petrographic grounds, but alternative deeper basinal inputs cannot be excluded.

The sulphur isotope composition of the celestine provides information on the evolution of the sulphate reservoir. The measured $\delta^{34}S$ values of the Jabal Hafit celestine range from +27.28‰ to +29.08‰ (mean +28.38‰) (Table 1). While the initial sulphate source was likely inherited from the dissolution of contemporaneous Paleogene evaporites or Oligocene seawater, which exhibit baseline Tertiary $\delta^{34}S$ values of 19.4‰–22.7‰ [35,36], simple inheritance cannot account for the observed isotopic signature.

Instead, the significant enrichment of approximately +5‰ to +8‰ is characteristic of Bacterial Sulphate Reduction (BSR) operating within a closed or semi-closed diagenetic environment [37,38]. During this process, sulphate-reducing bacteria preferentially metabolise the lighter ^{32}S isotope. Through Rayleigh-type closed-system fractionation, the residual dissolved sulphate pool becomes progressively enriched in ^{34}S, locking this heavy signature into the precipitating celestine [39].

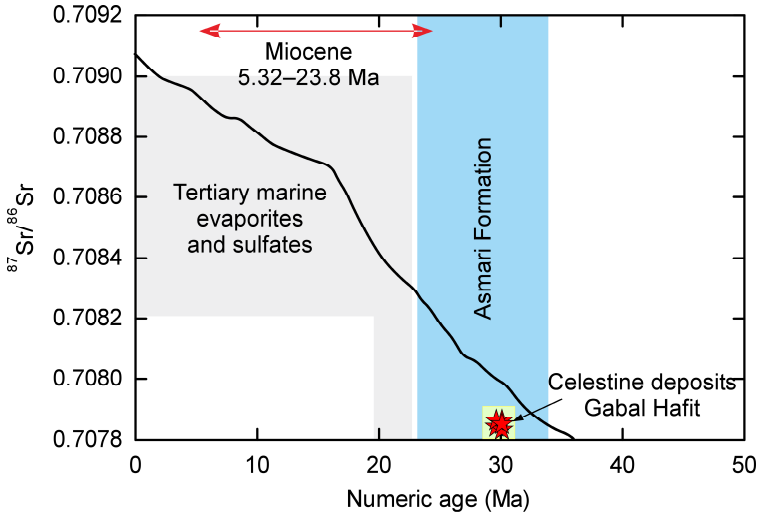

Figure 7. Comparison of celestine $^{87}Sr/^{86}Sr$ values with the marine Sr-isotope reference field [14], showing overlap with the Oligocene interval of the Asmari host succession. This overlap is interpreted as source compatibility, not as a unique crystallisation age.

Pyrite was not observed in the hand sample or thin section; however, this absence does not preclude BSR. Rather, it indicates an Fe-limited diagenetic system [40]. The Jabal Hafit sequence is dominated by high-purity carbonates where reactive iron is notably scarce, as confirmed by the minimal iron content in associated dolomite (Fe = 0.009–0.015 apfu; Supplementary Table S2). Without available iron to scavenge biogenically produced H_2S, visible sulphide mineralisation is muted or entirely inhibited. The generated H_2S likely migrated out of the system, leaving the ^{34}S-enriched residual sulphate behind.

Isotopic modification alone is insufficient to account for celestine saturation because modern seawater is generally undersaturated with respect to celestite, implying that precipitation required additional Sr enrichment, sulphate drawdown, or both. In the Jabal Hafit system, trace Sr contents in associated calcite and dolomite suggest that carbonate recrystallisation may have released Sr into pore fluids, while minor gypsum or anhydrite dissolution together with evaporative concentration could have modified sulphate availability and fluid salinity. Therefore, celestine may precipitate from burial brines that interacted with the host carbonates and underwent microbial modification of the sulphate reservoir.

4.4. Diagenetic Model and Comparison with Global Celestine Deposits

The integration of field relations, microtextures, mineral chemistry and isotopic data indicates that celestine at Jabal Hafit formed after initial lithification of the Asmari host, during early-to-mid burial diagenesis (Figure 8). The occurrence of large euhedral crystals in open vugs, fracture-hosted celestine and gypsum, and limestone–gypsum clasts within the mineralised horizon requires a brittle, at least partially cemented host rather than syn-depositional precipitation in unlithified sediment.

The paragenetic sequence inferred from petrography is: (1) the deposition of Asmari carbonates; (2) early calcite cementation, dolomitisation and local creation of a brittle host; (3) the development of fractures and vuggy secondary porosity during shallow burial; (4) the ingress of marine-derived or marine-buffered Sr-bearing brines; (5) limited BSR and associated enrichment of residual sulphate in ^{34}S; and (6) the precipitation of celestine, locally accompanied by fibrous gypsum, in available open space. This sequence reconciles the observed lithified-host textures with the low-temperature geochemical character of the deposit.

The geochemical characteristics and formation conditions of celestine from Jabal Hafit show significant similarities to other globally recognised celestine deposits, particularly in the Mediterranean and Middle Eastern basins, suggesting common diagenetic pro-

cesses that influenced its mineralisation (Table 2). The Jabal Hafit deposit exhibits distinct isotopic signatures compared to other Tethyan realm occurrences. Its strontium ratios (0.70784–0.70785, Table 1) are notably less radiogenic than the subsurface Miocene evaporites of Abu Dhabi (0.7084–0.7087; Ref. [8]), supporting the conclusion that the Sr was sourced from a remobilised Oligocene reservoir rather than contemporaneous Miocene seawater. Furthermore, the $\delta^{34}S$ values at Jabal Hafit (+28.4‰ avg; Table 1) represent a significantly higher degree of $\delta^{34}S$ enrichment than the Montevive (+19 to +21‰; Ref. [9]) and Likak (+20 to +22‰; Ref. [6]) deposits. This suggests that the diagenetic system at Jabal Hafit was more restricted, favouring more intensive bacterial sulphate reduction. Only the Mazraeh deposit in Iran [41] and the hydrothermal Huayingshan deposits in China [42] show comparable or higher $\delta^{34}S$ values. These features suggest a well-buffered fluid reservoir coupled with only modest, localised sulphate reduction. The deposit is therefore best viewed as a fracture-controlled, marine-buffered diagenetic end member rather than as an unequivocally hydrothermal or late tectonic system.

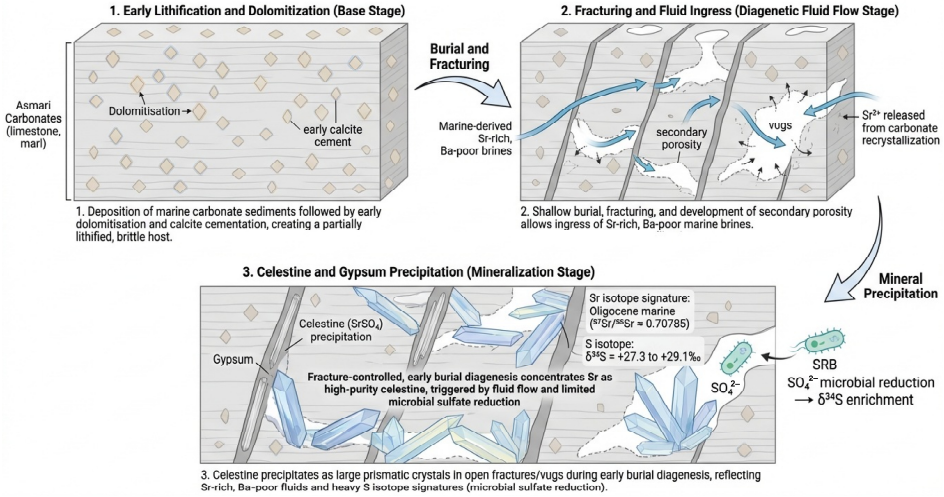

Figure 8. Conceptual model for the diagenetic formation of celestine at Jabal Hafit. The model emphasises post-lithification, fracture-controlled burial diagenesis, marine-buffered fluid flow, Sr loading by carbonate recrystallisation and/or evaporite dissolution, and sulphur isotope modification by BSR.

Table 2. Comparison of Jabal Hafit celestine with major global deposits.

Deposit/Region	Age/Formation	Host Lithology	87Sr/86Sr	δ34S (‰)	Formation Model
Jabal Hafit (UAE) (this study)	Oligocene (Asmari)	Limestone/ Dolomite	0.70784–0.70785	+27.3 to +29.1	Early burial diagenesis; Sr-rich marine brines.
Abu Dhabi (UAE) [8]	Miocene (Gachsaran)	Gypsum/ Anhydrite	0.7084–0.7087	+17.1 to +21.6	Marine coastal sabkha brines.
Montevive (Spain) [9,43]	U. Miocene (Messinian)	Gypsum/ Halite	~0.7082	+19 to +21	Shallow diagenetic replacement by Sr-$CaCl_2$ brines.
Likak (Iran) [6]	E.-M. Miocene (Gachsaran)	Evaporitic Limestone	0.7079–0.7080	+20 to +22	Late diagenetic sabkha brines; gypsum replacement.
Mazraeh (Iran) [41]	Oligo-Miocene (Qom)	Carbonate–Sabkha	0.7078–0.7081	+17 to +30	Early diagenetic replacement of limestone.
Shizilishan (China) [29]	Late Permian	Carbonate–Evaporite	0.7076–0.7079	+18 to +22	Sabkha diagenesis; non-marine brine; BSR.
Huayingshan (China) [42]	Triassic (Jialingjiang)	Marine Limestone	0.7076–0.7078	+36.4 to +39.0	Hydrothermal replacement of gypsum by hot brines.
San Augustin (Mexico) [44]	Cretaceous	Evaporite/ Carbonate	~0.7080	~+21	Epigenetic MVT-style replacement.
Severn side (UK) [45]	Triassic (Keuper)	Gypsum/ Red Beds	~0.7080	+23 to +27	Diagenetic replacement in red beds.

4.5. Economic Geology and Future Exploration

The Jabal Hafit celestine deposit represents a significant, yet under-explored, strontium resource within the UAE. The mineralogical data demonstrate high stoichiometric purity (>95% $SrSO_4$), meeting industrial specifications for conversion to Sr carbonate and related products [4]. Globally, demand for Sr is sustained by its applications in ferritic ceramic magnets, drilling fluids, pyrotechnics and specialised electronic and glass industries [27]. The burial-diagenetic, marine-derived model established here places Jabal Hafit within the broader class of sediment-hosted carbonate–evaporite celestine deposits formed by the circulation of Sr-rich, Ba-poor brines through permeable carbonate successions [1,12]. The demonstrated efficiency of Sr remobilisation and concentration into discrete cavity-filling $SrSO_4$ phases highlights the potential for economically meaningful enrichment where fluid flow was structurally controlled.

Future exploration should target major anticlinal structures where the Asmari–Lower Fars interface experienced tectonic fracturing, dolomitisation and anhydrite dissolution, conditions favourable for Sr-rich brine migration and celestine precipitation. Regional geochemical surveys focusing on ^{34}S-enriched sulphate in groundwater or residual soils may serve as effective pathfinders for concealed mineralisation, reflecting isotopic evolution of the sulphate reservoir.

5. Conclusions

The Jabal Hafit celestine mineralisation is best interpreted as a post-lithification burial-diagenetic concentration of Sr within Asmari carbonates. Integrated petrography, mineral chemistry and isotope systematics show that celestine precipitation was structurally and stratigraphically controlled, occurring in fractures and vugs developed after lithification of the host carbonate.

The near-stoichiometric composition of celestine, coupled with extremely low Ba incorporation, confirms precipitation from Sr-rich, Ba-depleted brines that had undergone prior barite removal. The negligible Sr content of associated calcite and ferroan dolomite indicates that the carbonate host acted as a plausible transient Sr reservoir, with subsequent diagenetic recrystallisation concentrating Sr into discrete sulphate phases. This highlights the efficiency of fluid-mediated trace-element redistribution in platform carbonates and demonstrates that economically meaningful Sr enrichment can develop without any requirement for external hydrothermal input.

The $^{87}Sr/^{86}Sr$ data show that the mineralising fluid carried a uniform, marine-like Oligocene Sr signature, but they do not resolve meaningful inter-sample variation or provide a unique crystallisation age. Elevated $\delta^{34}S$ values indicate isotopic evolution of the sulphate reservoir, plausibly through bacterial sulphate reduction in a semi-closed pore system. Celestine supersaturation therefore most likely required Sr enrichment by carbonate recrystallisation and/or evaporitic concentration in addition to sulphur isotope modification. Jabal Hafit thus represents a marine-buffered burial-diagenetic celestine system with a relatively heavy sulphate isotope signature.

Supplementary Materials: The following supporting information can be downloaded at: https://www.mdpi.com/article/10.3390/min16060575/s1, Figure S1. XRD charts shows the high purity celestine from Jabal Hafit, Al-Ain, United Arab Emirates; Table S1. Chemical composition of celestine from Jabal Hafit, Al-Ain (UAE); Table S2: Chemical composition of calcite and dolomite from Jabal Hafit, Al-Ain (UAE).

Author Contributions: Conceptualisation, M.S., B.M.A., I.V.S. and M.R.A.; methodology, M.S., B.M.A., I.V.S., C.-F.L. and M.R.A.; software, M.S. and D.F.; validation, M.S., B.M.A., I.V.S., C.-F.L. and M.R.A.; formal analysis, M.S., B.M.A., I.V.S. and M.R.A.; investigation, M.S., B.M.A., A.A.-A.,

M.A. (Maryam Alali), M.M., M.A. (Mariam Aldhaheri), A.A., S.S.A. and D.F.; resources, M.S., I.V.S., C.-F.L. and M.R.A.; data curation, M.S., B.M.A., A.A.-A., M.A. (Maryam Alali), M.M., M.A. (Mariam Aldhaheri), A.A., and D.F.; writing—original draft preparation, M.S. and D.F.; writing—review and editing, M.S., B.M.A., I.V.S., C.-F.L. and D.F.; visualization, M.S., B.M.A., M.M. and D.F.; supervision, M.S. and B.M.A.; project administration, M.S. and B.M.A.; funding acquisition, M.S., I.V.S. and S.S.A. All authors have read and agreed to the published version of the manuscript.

Funding: This study was financially supported by SURE Plus grants (G00004879) from the United Arab Emirates University, UAE. Sincere thanks and gratitude to the Ongoing Research Funding Program (ORF-2026-1459), King Saud University, Riyadh, Saudi Arabia, for funding this research article.

Data Availability Statement: Data are contained within the article and Supplementary Materials.

Acknowledgments: We sincerely appreciate the insightful comments and constructive suggestions offered by the anonymous reviewers and the editor. Their feedback greatly improved the clarity of the manuscript and the data interpretation. We would like to thank the Environmental Agency–Abu Dhabi (UAE) for their support and help in collecting the celestine samples. During the preparation of this manuscript, the authors used AI for assistance with drafting, language editing, and improving the clarity and organisation of the manuscript text. The authors critically reviewed, revised, and validated all generated content and take full responsibility for the final content of the manuscript. The authors have reviewed and edited the output and take full responsibility for the content of this publication.

Conflicts of Interest: The authors declare no conflicts of interest.

References

1. Hanor, J.S. A model for the origin of large carbonate-and evaporite-hosted celestine ($SrSO_4$) deposits. *J. Sediment. Res.* **2004**, *74*, 168–175. [CrossRef]
2. Bjørlykke, K. Relationships between depositional environments, burial history and rock properties. Some principal aspects of diagenetic process in sedimentary basins. *Sediment. Geol.* **2014**, *301*, 1–14. [CrossRef]
3. Taberner, C.; Marshall, J.D.; Hendry, J.P.; Pierre, C.; Thirlwall, M. Celestite formation, bacterial sulphate reduction and carbonate cementation of Eocene reefs and basinal sediments (Igualada, NE Spain). *Sedimentology* **2002**, *49*, 171–190. [CrossRef]
4. Hanor, J.S. Barite–celestine geochemistry and environments of formation. *Rev. Mineral. Geochem.* **2000**, *40*, 193–275. [CrossRef]
5. Esteves, B.F.; Spielman-Sun, E.; Li, Q.; Jew, A.D.; Bargar, J.R.; Druhan, J.L. Geochemical Modeling of Celestite ($SrSO_4$) Precipitation and Reactive Transport in Shales. *Environ. Sci. Technol.* **2022**, *56*, 4336–4344. [CrossRef]
6. Ehya, F.; Shakouri, B.; Rafi, M. Geology, mineralogy, and isotope (Sr, S) geochemistry of the Likak celestite deposit, SW Iran. *Carbonates Evaporites* **2013**, *28*, 419–431. [CrossRef]
7. Fathy, D.; Farouk, S.; Qteishat, A.; Ahmad, F.; Sami, M.; Al-Kahtany, K.; Lee, E.Y. Geochemical characterization of Upper Cretaceous organic-rich deposits: Insights from the Azraq Basin in Jordan. *J. Asian Earth Sci.* **2024**, *276*, 106365. [CrossRef]
8. Gad, A.; Abdelghany, O.; Arman, H.; Mahmoud, B.; Aldahan, A.; Paramban, S.; Saima, M.A. Geochemistry and Sr, S, and O stable isotopes of Miocene Abu Dhabi evaporites, United Arab Emirates. *Heliyon* **2023**, *9*, e16033. [CrossRef] [PubMed]
9. García-Veigas, J.; Rosell, L.; Cendón, D.I.; Gibert, L.; Martín, J.M.; Torres-Ruiz, J.; Orti, F. Large celestine orebodies formed by early-diagenetic replacement of gypsified stromatolites (Upper Miocene, Montevive–Escúzar deposit, Granada Basin, Spain). *Ore Geol. Rev.* **2015**, *64*, 187–199. [CrossRef]
10. Fathy, D.; Wagreich, M.; Sami, M. *Geochemical Evidence for Photic Zone Euxinia During Greenhouse Climate in the Tethys Sea, Egypt*; Springer International Publishing: Cham, Switzerland, 2022; pp. 373–374.
11. Hryniv, S.; Peryt, T.M. Strontium distribution and celestite occurrence in Zechstein (Upper Permian) anhydrites of West Poland. *Geochemistry* **2010**, *70*, 137–147. [CrossRef]
12. Ortí, F.; Pérez-López, A.; García-Veigas, J.; Rosell, L.; Cendón, D.I.; Pérez-Valera, F. Sulfate isotope compositions (δ34S, δ18O) and strontium isotopic ratios (87Sr/86Sr) of Triassic evaporites in the Betic Cordillera (SE Spain). *Rev. Soc. Geol. Esp.* **2014**, *27*, 79–90.
13. McArthur, J.; Howarth, R.J. Sr-isotope stratigraphy: The Phanerozoic 87 Sr/ 86 Sr-curve and explanatory notes. In *A Geological Timescale*; Cambridge University Press: Cambridge, UK, 2004; pp. 96–105.
14. McArthur, J.M.; Howarth, R.; Bailey, T. Strontium isotope stratigraphy: LOWESS version 3: Best fit to the marine Sr-isotope curve for 0–509 Ma and accompanying look-up table for deriving numerical age. *J. Geol.* **2001**, *109*, 155–170. [CrossRef]
15. Hansman, R.J.; Ring, U. Jabal Hafit anticline (UAE and Oman) formed by décollement folding followed by trishear fault-propagation folding. *J. Struct. Geol.* **2018**, *117*, 168–185. [CrossRef]

16. El-Sayed, M.I. Karastic features associated with unconformity surfaces, a case study from the United Arab Emirates. *J. Arid. Environ.* **2000**, *46*, 295–312. [CrossRef]
17. El Tokhi, M.; Arman, H.; Abdelghany, O.; Hashem, W.; El Saiy, A. Isotope Stratigraphy of Oligocene Limestone in Al-Ain City, United Arab Emirates. *Arab. J. Sci. Eng.* **2012**, *37*, 1439–1449. [CrossRef]
18. Ehrenberg, S.; Pickard, N.; Laursen, G.; Monibi, S.; Mossadegh, Z.; Svånå, T.; Aqrawi, A.; McArthur, J.; Thirlwall, M. Strontium Isotope Stratigraphy of the Asmari Formation (Oligocene-Lower Miocene), SW Iran. *J. Pet. Geol.* **2007**, *30*, 107–128. [CrossRef]
19. Al Farraj, A.; Harvey, A.M. Late Quaternary interactions between aeolian and fluvial processes: A case study in the northern UAE. *J. Arid. Environ.* **2004**, *56*, 235–248. [CrossRef]
20. Abd-Allah, A.M.; Hashem, W.A.; Abdelghany, O. Structural and tectonostratigraphic evolution of the upper cretaceous–eocene sequence in Malaqet–Mundassah–El Saah range, Oman mountains, United Arab Emirates and Oman. *J. Afr. Earth Sci.* **2013**, *79*, 111–124. [CrossRef]
21. Sami, M.; Gamaleldien, H.; Ntaflos, T.; Li, C.-F.; Sanislav, I.V.; Zhao, X.; Kamaunji, V.D.; Mahmoud, B.; Fathy, D.; Abukhadra, M.R.; et al. Geochemical constraints on the evolution and tectonic setting of United Arab Emirates Ophiolitic Serpentinites. *J. Asian Earth Sci.* **2026**, *300*, 106990. [CrossRef]
22. Abdelghany, O. Biostratigraphy (Turborotalia cunialensis/Cribrohantkenina inflata concurrent-range zone, P16) of the late Eocene dammam formation, west of the Northern Oman Mountains. *Micropaleontology* **2002**, *48*, 209–221. [CrossRef]
23. Agard, P.; Omrani, J.; Jolivet, L.; Whitechurch, H.; Vrielynck, B.; Spakman, W.; Monié, P.; Meyer, B.; Wortel, R. Zagros orogeny: A subduction-dominated process. *Geol. Mag.* **2011**, *148*, 692–725. [CrossRef]
24. Arman, H.; Hashem, W.; El Tokhi, M.; Abdelghany, O.; El Saiy, A. Petrographical and geomechanical properties of the Lower Oligocene limestones from Al Ain city, United Arab Emirates. *Arab. J. Sci. Eng.* **2014**, *39*, 261–271. [CrossRef]
25. Forjanes, P.; Gómez-Barreiro, J.; Morales, J.; Astilleros, J.M.; Fernández-Díaz, L. Epitactic growth of celestite on anhydrite: Substrate induced twinning and morphological evolution of aggregates. *CrystEngComm* **2020**, *22*, 5743–5759. [CrossRef]
26. Choquette, P.W.; Pray, L.C. Geologic nomenclature and classification of porosity in sedimentary carbonates. *AAPG Bull.* **1970**, *54*, 207–250. [CrossRef]
27. Wang, A.; Wang, Z.; Liu, J.; Xu, N.; Li, H. The Sr/Ba ratio response to salinity in clastic sediments of the Yangtze River Delta. *Chem. Geol.* **2021**, *559*, 119923. [CrossRef]
28. Hawthorne, F.C.; Krivovichev, S.V.; Burns, P.C. The crystal chemistry of sulfate minerals. *Rev. Mineral. Geochem.* **2000**, *40*, 1–112. [CrossRef]
29. Zhu, Q.; Cook, N.J.; Xie, G.; Ciobanu, C.L.; Gilbert, S.E.; Wade, B.; Xu, J. Textural and geochemical analysis of celestine and sulfides constrain Sr-(Pb-Zn) mineralization in the Shizilishan deposit, eastern China. *Ore Geol. Rev.* **2022**, *144*, 104814. [CrossRef]
30. Xu, H.; Zhang, W.; Wei, K.; He, Q.; Jiang, Y.; Xu, T.; Jiang, X.; Yan, G.; Song, H.; Wang, J. Ferroan dolomites in Miocene sediments of the Xisha Islands and their genetic model. *J. Oceanol. Limnol.* **2018**, *36*, 165–180. [CrossRef]
31. Vahrenkamp, V.C.; Swart, P.K. New distribution coefficient for the incorporation of strontium into dolomite and its implications for the formation of ancient dolomites. *Geology* **1990**, *18*, 387–391. [CrossRef]
32. Marenco, P.J.; Corsetti, F.A.; Kaufman, A.J.; Bottjer, D.J. Environmental and diagenetic variations in carbonate associated sulfate: An investigation of CAS in the Lower Triassic of the western USA. *Geochim. Cosmochim. Acta* **2008**, *72*, 1570–1582. [CrossRef]
33. Present, T.M.; Paris, G.; Burke, A.; Fischer, W.W.; Adkins, J.F. Large Carbonate Associated Sulfate isotopic variability between brachiopods, micrite, and other sedimentary components in Late Ordovician strata. *Earth Planet. Sci. Lett.* **2015**, *432*, 187–198. [CrossRef]
34. Schurr, S.L.; Strauss, H.; Mueller, M.; Immenhauser, A. Assessing the robustness of carbonate-associated sulfate during hydrothermal dolomitization of the Latemar platform, Italy. *Terra Nova* **2021**, *33*, 621–629. [CrossRef]
35. Utrilla, R.; Pierre, C.; Orti, F.; Pueyo, J.J. Oxygen and sulphur isotope compositions as indicators of the origin of Mesozoic and Cenozoic evaporites from Spain. *Chem. Geol.* **1992**, *102*, 229–244. [CrossRef]
36. Paytan, A.; Kastner, M.; Campbell, D.; Thiemens, M.H. Sulfur isotopic composition of Cenozoic seawater sulfate. *Science* **1998**, *282*, 1459–1462. [CrossRef]
37. Torfstein, A.; Turchyn, A.V. Rates and Cycles of Microbial Sulfate Reduction in the Hyper-Saline Dead Sea over the Last 200 kyrs from Sedimentary δ34S and δ18O (SO 4). *Front. Earth Sci.* **2017**, *5*, 62. [CrossRef]
38. Abdelhady, A.A.; Seuss, B.; Jain, S.; Fathy, D.; Sami, M.; Ali, A.; Elsheikh, A.; Ahmed, M.S.; Elewa, A.M.; Hussain, A.M. Molecular technology in paleontology and paleobiology: Applications and limitations. *Quat. Int.* **2024**, *685*, 24–38. [CrossRef]
39. Habicht, K.S.; Canfield, D.E. Isotope fractionation by sulfate-reducing natural populations and the isotopic composition of sulfide in marine sediments. *Geology* **2001**, *29*, 555–558. [CrossRef]
40. Machel, H.G. Bacterial and thermochemical sulfate reduction in diagenetic settings—Old and new insights. *Sediment. Geol.* **2001**, *140*, 143–175.
41. Ranjbaran, M.; Moghaddasi, S.J.; Sotohian, F.; Guilan, I. Study of texture the Mazraeh celestite deposit from North Central Iran. *J. Tethys* **2014**, *2*, 20–28.

42. Gao, Y.; Sun, Y.; Wang, D.; Chen, B.; Gu, W. Geological and geochemical constraints on the origin of the Sr mineralization in Huayingshan ore district, Chongqing, South China. *Minerals* **2023**, *13*, 279. [CrossRef]
43. Ariza-Rodríguez, N.; Rodríguez-Navarro, A.B.; Calero de Hoces, M.; Martin, J.M.; Muñoz-Batista, M.J. Chemical and mineralogical characterization of montevive celestine mineral. *Minerals* **2022**, *12*, 1261. [CrossRef]
44. González-Sánchez, F.; Camprubí, A.; González-Partida, E.; Puente-Solís, R.; Canet, C.; Centeno-García, E.; Atudorei, V. Regional stratigraphy and distribution of epigenetic stratabound celestine, fluorite, barite and Pb–Zn deposits in the MVT province of northeastern Mexico. *Miner. Depos.* **2009**, *44*, 343–361. [CrossRef]
45. Wood, M.; Shaw, H. The geochemistry of celestites from the Yate area near Bristol (UK). *Chem. Geol.* **1976**, *17*, 179–193. [CrossRef]